Photocurrent spectroscopy of bound-to-bound intraband transitions in GaN/AlN quantum dots

A. Vardi* and G. Bahir
Department of Electrical Engineering, Technion-Israel Institute of Technology, Haifa 32000, Israel

S. E. Schacham
Department of Electrical and Electronic Engineering, Ariel University Center, Ariel 40700, Israel

P. K. Kandaswamy and E. Monroy
Equipe Mixte CEA-CNRS "Nanophysique et Semiconducteurs", INAC/SP2M/NPSC, CEA-Grenoble, 17 rue des Martyrs, 38054 Grenoble Cedex 9, France

(Received 21 June 2009; revised manuscript received 23 August 2009; published 19 October 2009)

Using photocurrent infrared spectroscopy, we characterized bound-to-bound transitions in the conduction band of samples with high density of GaN/AlN quantum dots (QDs). TE (TM) polarized peaks at 0.15–0.23 eV (0.7–0.9 eV) depending on the dot size, are associated with S-$P_{x,y}$ (S-P_z) transitions. The transition energies and the oscillator strengths were analyzed by numerical solution of the Schrödinger equation in three dimensions for truncated hexagonal pyramid dots. Assuming peak broadening due to dot size fluctuations, we derived the dot dimensions for which all observed photocurrent peak energies can be accounted for. It is shown that for these dimensions to agree with the quantum well limit both nonparabolicity and anisotropy of the conduction band must be taken into account. The appearance of photocurrent due to bound-to-bound intraband transitions within the QDs is attributed to lateral hopping conductivity. Analysis of the photoresponse magnitude due to optical excitation of electrons to different states in the QD yields a two-dimensional mobility edge at ~1 eV above the GaN conduction-band edge. The hopping model is further supported by the temperature dependence of the dark conductivity and its sensitivity to the size and the density of the QDs.

DOI: 10.1103/PhysRevB.80.155439 PACS number(s): 78.67.Hc, 73.63.Kv, 72.40.+w, 72.80.Ey

I. INTRODUCTION

Quantum dots (QDs) based on a variety of semiconductor compounds have attracted considerable interest in the past few years due to their unique physical properties as well as their potential applications for improving solid-state lasers[1,2] or for the fabrication of controlled single-photon emitters.[3] Epitaxially grown GaN QDs embedded in AlN open a new spectral region of blue and ultraviolet for high-temperature single-photon sources. In this material system the possibility of observing single-photon emission close to room temperature[4] is a direct consequence of strong carrier localization due to the large band offset (up to 1.8 eV between GaN and AlN). Another appealing feature of GaN/AlN QDs, also stemming from the large band offset, is the appearance of intersubband (ISB)/intraband (IB) transitions in the near-infrared (NIR) spectral range (1–3 μm).[5] Pushing ISB/IB devices to the NIR range using AlN/GaN heterostructures is of great interest as the material properties of III nitrides combined with the inherent features of ISB devices can lead to unique devices for NIR applications such as high-power tunable lasers for medical spectroscopy,[6] as well as high-speed modulators and detectors. Indeed, in the last years there were several demonstrations of devices based on ISB transitions in GaN/AlN structures, including all-optical switches,[7] electro-optical modulators,[8] lateral quantum dot IR photodetectors[9] (QDIPs) and quantum cascade detectors.[10] Despite substantial progress in the synthesis of nitride semiconductor heterostructures, there are still large uncertainties in the nitride material parameters, in particular, the effective masses and the static polarization, which have a major effect on the physical properties of the structure. The implementation of efficient III-nitride-based ISB devices depends on the understanding of both the electronic spectrum and the various carrier transport mechanisms.

Most ISB devices rely on vertical carrier transport, in which photoexcited carriers in the continuum are drifted by the electric field along the growth direction.[11] Thus, in QD-based devices, photocurrent is usually generated by transitions from bound states in the QDs to extended states in the wetting layer (WL) or in the continuum. Photocurrent related to bound-to-bound (BtB) electronic transition is not likely since the excited-state energies are below the effective potential barrier and excited carriers have a low escape probability.[12]

A device configuration relying on in-plane transport between QDs can be useful to study the in-plane QD coupling mechanisms and provide an insight to the QD electronic structure. In-plane conductance between individual QDs was observed in the InAs/GaAs material system[13] as well as in Si/Ge QDs.[14] Due to carrier localization in these systems, the main lateral transport mechanism, at sufficiently low temperatures, is variable range hopping (VRH).[15] In VRH, the carrier may optimize their paths in a four dimensional space of energy (E) and real space (x,y,z), referred to as the *range*. This type of transport is highly sensitive to the energy level of optically excited carriers and hence can provide an instrument to assess the energy-level distribution in the QDs. Since IB transitions in the conduction band of GaN/AlN QDs occur in the infrared spectral range whereas interband transition is at UV wavelengths (3.5–5 eV), it is a relatively easy task to assure that the samples are excited by light that can only cause IB transitions in the QDs.

In this work we characterize the polarization-dependent mid-IR (MIR) photoresponse of lateral QDIPs at low temperature ($T \approx 12$ K) in order to identify the energy levels in the QD conduction band. The appearance of photoresponse at energies lower than the effective barrier height is attributed to the increase in hopping probability following BtB excitation in the QDs. By combination of photocurrent spectroscopy and theoretical models for the absorption and lateral transport, we present a consistent picture of the IB transitions within the QDs and the sensitivity of transport properties to the size and the density of the QDs and to the levels into which carriers are excited. The paper is organized as follows. In Sec. II, the sample structures and the experimental setup are introduced. The experimental results are presented in Sec. III. In Sec. IV, the single-band effective-mass three-dimensional (3D) model for IB transitions is described. This model is applied to interpret the experimental IB photocurrent spectra, focusing on the relations between QD dimensions, mass tensor, and transitions energies. Finally, the photocurrent and the dark current are analyzed based on the hopping model.

II. EXPERIMENTAL

Two samples were studied: E697 and E645, containing dots of different dimensions. Both samples consist of 20 periods of GaN QD layers with 3-nm-thick AlN spacers, grown by plasma-assisted molecular beam epitaxy (PAMBE) on 1-μm-thick AlN-on-sapphire (0001) templates. During the deposition of the QDs, Si doping was introduced in the nominal level of 10^{20} cm^{-3}. High-resolution transmission electron microscopy (HRTEM) shows that the QDs are truncated hexagonal pyramids with $\{10\bar{1}3\}$ facets formed over a WL of about two monolayers[16] and no Ga-Al interdiffusion has been observed.[17] To characterize the QD size and the density using atomic force microscopy (AFM), an additional QD layer was deposited on the surface. More details on the sample growth and characterization can be found in Ref. 18. A 400×400 nm^2 AFM image of the samples is presented in Fig. 1; the size and the density of QDs extracted from AFM are summarized in Table I. The large error margins in the QD dimensions translate the effect of the apex size of the AFM probe on the measurements. In both samples there is a large fluctuation in the QDs lateral dimension around a constant aspect ratio (height to base diameter ratio). This aspect ratio to some extent depends on the growth conditions[18] but typically it is about 1/5 in GaN/AlN QDs.[16]

In order to further establish the differences in the QD dimensions between the two samples, in addition to the AFM characterization, we performed photoluminescence (PL) and NIR transmittance measurements. For PL measurements, we used the dispersed light of a xenon lamp as the excitation source. The NIR transmittance measurements were conducted in a wedge-multipass waveguide configuration, using a commercial InSb detector. The samples show P polarized absorption peak in the NIR, which is associated with the transition from the ground state S to the first excited level with two antinodes along the growth direction, P_z. This peak was well characterized in previous analysis performed on similar structures.[9] Here, we only state the relevant results for the two discussed samples. Table I summarizes the results.

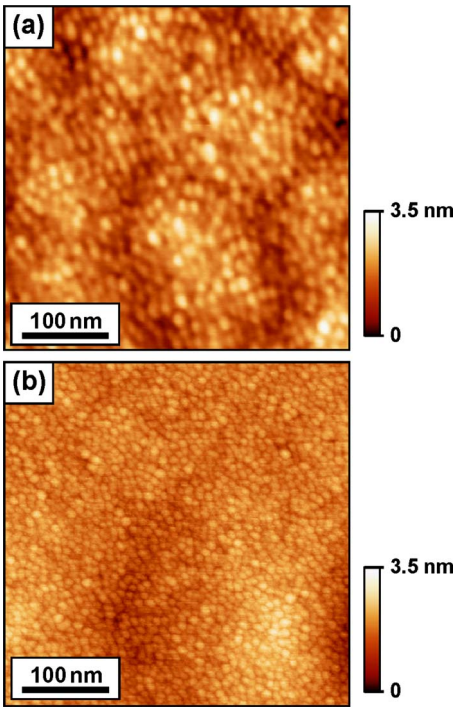

FIG. 1. (Color online) AFM images of samples (a) E697 and (b) E645 showing the different QD sizes and densities.

The critical dimension of the QDs is in the growth direction (height), which is considerably smaller than the lateral dimensions (diameter). Thus, both the PL and the S-P_z energies are associated mostly with the QD height. The difference in the energies of the PL peaks is a clear evidence of the size difference between the two samples. In both samples the PL peak is blueshifted with respect to bulk GaN (3.5 eV); but in sample E645, which contains smaller QDs, the blueshift is larger due to a stronger quantum confinement. The small full width at half maximum (FWHM) of the PL and the S-P_z transition indicates excellent homogeneity of the QD height (roughness of less than ± 0.5 nm) in both samples. The S-P_z transition, deduced from the NIR transmittance measurements, also reflects the size difference between the two samples but more importantly it contains information on the actual electron density in the QDs. To estimate the effective electron density in the QDs, we used the following expression describing the QD sheet absorption coefficient ($\alpha \ll 1$) for an IB transition from a state g to a final state e in the QD (Ref. 19):

$$\alpha_{ge}^{2D} = \frac{\pi N_d e^2}{2 m_0 \varepsilon_0 n c} G(\omega - \omega_{ge})(N_g - N_e)\Theta_{ge}, \tag{1}$$

where N_d is areal density of absorbing QDs; Θ_{ge} is the oscillator strength (OS); and N_g and N_e are the occupation probabilities of the initial and the final states, respectively. m_0 is the electron rest mass, c is the speed of light, n is the index of refraction, and ε_0 is the permeability. $G(\omega - \omega_{ge})$ is

TABLE I. Results of sample characterization by photoluminescence, IR absorption, and AFM.

Sample	PL peak (FWHM) (eV)	S-P_z (FWHM) (eV)	Absorption per pass (%)	Areal density (10^{11} cm^{-2})	QD diameter (nm)	QD height (nm)
E645	3.83 (0.15)	0.83 (0.1)	0.5	12 ± 1	11 ± 2	1.3 ± 0.6
E697	3.63 (0.25)	0.75 (0.15)	1.15	4.6 ± 5	16 ± 3	1.3 ± 0.6

the line-shape function which takes the form of a Lorentzian in the ideal case where only lifetime broadening is present. In the case of self-assembled QDs, the size distribution of the QD introduces inhomogeneous broadening to the ensemble absorption line, and the line shape becomes Gaussian.[20] Using Eq. (1), the S-P_z ($g=S$ and $e=P_z$) absorption $\alpha^{2D}_{S\text{-}P_z}$ can be evaluated and compared with the experimental results. Assuming, N_S close to unit, $N_{P_z} \cong 0$, the absorption at the S-P_z resonance is $0.17N_d$ [10^{12} cm^{-2}]/FWHM [meV], where the GaN material parameters were assumed to be $m^*=0.2m_0$ and $n=2.3$ (in the NIR)[21] and the S-P_z OS was numerically evaluated (see Sec. IV A) as $\Theta_{S\text{-}P_z} \simeq 0.75m_0/m^*$. Using the QD density deduced by AFM and the measured absorption per pass of the S-P_z transition, the above expression yields fill factors of 1/8 and 1/1 electrons per dot for samples E645 and E697, respectively. This means that, at sufficiently low temperatures, only the ground state of the QDs is occupied.

In order to fabricate QDIPs based on in-plane transport, standard photolithography and dry etching techniques were used to define an etched interdigitated contact structure down to the AlN buffer. Ti/Al/Ti/Au contacts were deposited into the etched contact channel using self-aligned and lift-off technique. The ten contact fingers formed were 800 μm long, 20 μm wide, and 10–20 μm apart. This structure was designed in order to maximize the active region while maintaining relatively large electric field.

Conductivity measurements were performed using an HP 4155B semiconductor parameter analyzer. Photocurrent measurements were preformed using Fourier transform infrared analyzer (Bruker-Equinox 55) with a tungsten-halogen source for NIR (1–3 μm) and a glow bar for the MIR (3–15 μm). To allow for polarization analysis, the facets of the samples were polished in 45°. The IR spectral dependence was measured using a standard lock-in technique, in wedge and front illumination. It should be pointed out that the sapphire-substrate spectral cutoff is at 5.5 μm. In order to analyze the polarization at longer wavelengths in wedge configuration, the devices were fabricated as close as possible to the polished facets of the sample.

For reference, an additional sample was grown containing only PAMBE grown AlN on the same template [AlN-on-sapphire (0001)]. The sample was processed and measured under the exact same conditions as the other two samples, containing the QDs. The reference sample was not conductive and exhibited no photoresponse in the infrared spectral range.

III. EXPERIMENTAL RESULTS

The low-temperature ($T=12$ K) photocurrent spectra of the two samples in the MIR spectral range are presented in Fig. 2 for front illumination and 10 V bias (shown schematically in the inset). The photoresponse increases linearly with bias (between 0 and 10 V). Typical values of integrated photocurrent due to the glow bar illumination are in the range of 0.01 μA. Both samples exhibit photoresponse over the range of 0.1–0.3 eV, indicating that there is a large distribution in the lateral dimension of the QDs. However, the response peaks at different energies. This confirms that the difference in QD heights between the two samples—evident from the PL and the S-P_z absorption measurements—is accompanied by a difference in the average lateral dimensions. The spectral response in the small QD sample (E645) peaks at a higher energy due to stronger lateral confinement, consistent with the reduced base diameter extracted from the AFM images (Fig. 1 and Table I). As the photocurrent measurements were conducted in free space, sharp spectral dips are observed, associated with atmospheric absorption.

In order to characterize the polarization dependence of the spectra, we measured the response in a 45° wedge configuration [shown schematically in Fig. 3(a)]. Using a linear polarizer between the source and the wedge, it is possible to shine in-plane polarized light on the device (S polarization). P polarization is obtained by rotating the polarizer by 90° with respect to S polarization, resulting in a reduction in the intensity of the in-plane light component by a factor of 2. The intensity of the in-plane component follows $(1/2)\sin^2(\theta)+\cos^2(\theta)$, where θ is the angle of the polarizer at the wedge plane with respect to the S polarization. In this configuration, the absorption of the sapphire substrate (significant below 0.22 eV) must be taken into consideration. In sample E645 (small dots) the MIR peak energy is just above

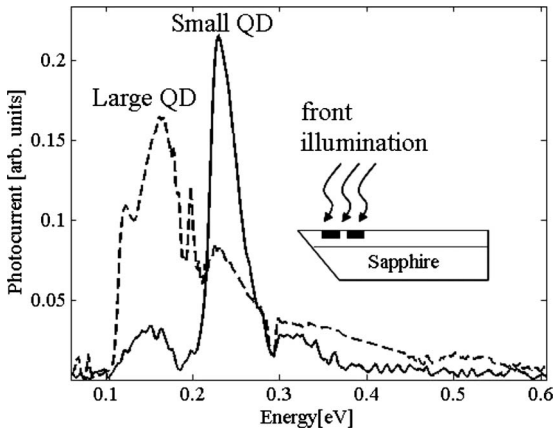

FIG. 2. Mid-IR spectral response of sample E645 (full line) and sample E697 (dash line) measured at $T \approx 12$ K under front illumination and 10 V bias. Sapphire cutoff is at 0.22 eV.

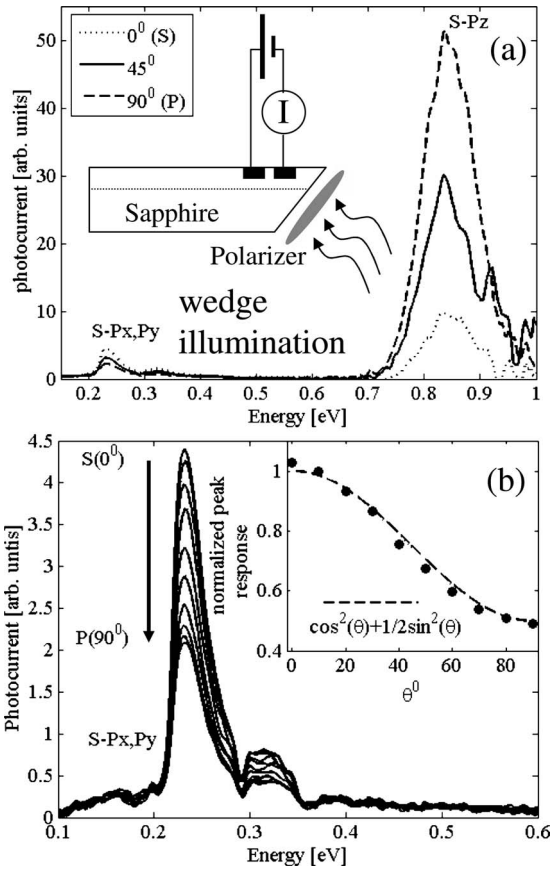

FIG. 3. Polarization-dependent spectral response of sample E645 measured in wedge illumination. (a) Normalized response of both S-P_z peak at near IR and S-P_x,P_y peak at mid-IR; S-P_z peak is 10 times larger than S-P_x,P_y peak. (b) Measurement of S-P_x,P_y peak as a function of polarizer angle. At 0° only in-plane component exists resulting in maximum response; at 90° with 50% of the light in-plane polarized, the response reduced by a factor of 2. All the spectra were normalized by the spectral intensity of the excitation source as measured by a flat spectral response calibrated detector.

this energy threshold while in sample E697 (large dots) it is well below it, resulting in a significantly attenuation of the MIR signal.

Figure 3(a) shows the spectral response of sample E645 measured in a wedge configuration at different polarizer angles. The measured spectra were normalized to the excitation spectral intensity as measured by a flat spectral response calibrated detector. The spectra show two distinct peaks: one at 0.23 eV, associated with the S-P_x,P_y transitions, and the other at 0.82 eV, assigned to the S-P_z transition. S-P_z is maximal in the case of P polarization and minimal for S polarization. In contrast, the S-P_x,P_y peak intensity drops approximately by a factor of 2 as the light polarization changes from S to P, as depicted in Fig. 3(b). The inset of Fig. 3(b) shows the fitting of the normalized intensity to the theoretical expression $(1/2)\sin^2(\theta)+\cos^2(\theta)$, demonstrating the TE nature of the 0.23 eV peak. The observation that the S-P_z transition retains 20% of the maximal power in S polarization is related to scattered light.

The simultaneous observation of both peaks, along with their polarization dependence, confirms that they are both due to IB transitions in the QD conduction band. The fact that the normalized response at 0.82 eV is an order of magnitude stronger than the response at 0.23 eV suggests that carriers in the P_z states are more mobile than those in the P_x,P_y states, as will be discussed in Sec. IV B.

IV. DISCUSSION

In this section we discuss the two main elements that govern the photocurrent response. The first element is the optical absorption and its polarization dependence. This aspect of the measurement requires an evaluation of the conduction-band energy levels along with the 3D wave functions. The other element is the transport of excited carriers in the QDs plane. Since the excited carriers energies are well below the two-dimensional (2D) quasicontinuum formed by the WL, models for lateral QDIPs (Refs. 22–24) cannot be applied, and transport theory for highly localized systems should be applied.

A. Calculation of the QD electronic structure and IB absorption

The optical transition from state a to any state a' in the system is governed by the OS given by the expression

$$\Theta_{a'a} = \frac{2}{m_0}\frac{|\langle a'|P|a\rangle|^2}{E_{a'a}}, \tag{2}$$

where $E_{a'a}$ is the transition energy and P is the momentum operator which dictates the selection rules of IB transitions. As in atoms, higher OS is associated with transitions from the ground state to the P shell. The polarization dependence is mainly due to the flatten shape of the QDs.[16] The stronger confinement in the growth direction splits the P shell, resulting in anisotropic absorption. Since in our QDs only the ground state is filled at low temperature, the S-to-P-shell transitions are the main transitions observed.

In order to evaluate the energy levels and the wave functions in the QD, we solved numerically the single-band Schrödinger equation in three dimensions with a constant effective mass, taking into account the hexagonal shape of the quantum dot. Extending the numerical method outlined in Ref. 25, a position- (material-) dependent effective mass (for GaN and for AlN) was introduced into the Schrödinger equation

$$\left(-\frac{\hbar^2}{2}\nabla\frac{1}{m^*_{e(hh)}(x,y,z)}\nabla + V_{e(hh)}(x,y,z)\right)\varphi_{e(hh)} = E\varphi_{e(hh)}, \tag{3}$$

where $\hbar$ is the reduced Planck's constant and $m^*_{e(hh)}$ is the electron (heavy-hole) effective mass. The total potential drop is given by $V_{e(hh)}=\Delta E_{c(v)}+\phi$, where $\Delta E_{c(v)}$ is the conduction- (valance-) band offset, ϕ is the potential due to the static polarization field in the structure, and $\varphi_{e(hh)}$ is the envelope part of the electron (heavy-hole) wave function. The conduction-band offset was taken as $\Delta E_c=1.8$ eV and

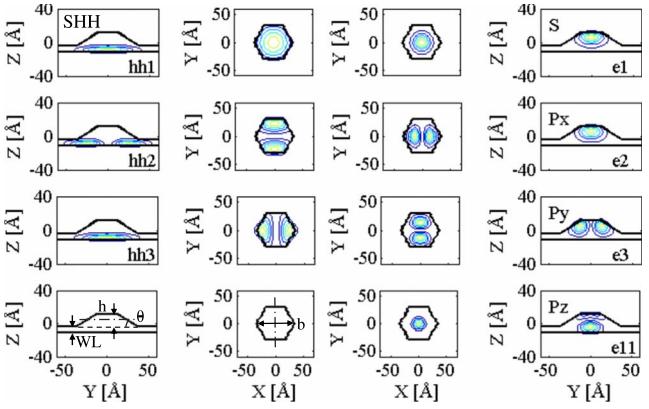

FIG. 4. (Color online) Contours of calculated 3D squared-absolute wave functions based on effective-mass approximation for $h=1.5$ nm and $b=8$ nm, in a cross-section through the QD center in Y-Z and in X-Y planes. The two columns on the right show electron wave functions (S, P_y, P_x, and P_z) and the two columns on the left show the first three states in valance band. h, b, θ, and WL are defined in two lowest left drawings showing cross sections through which wave functions are presented (dotted-dashed line).

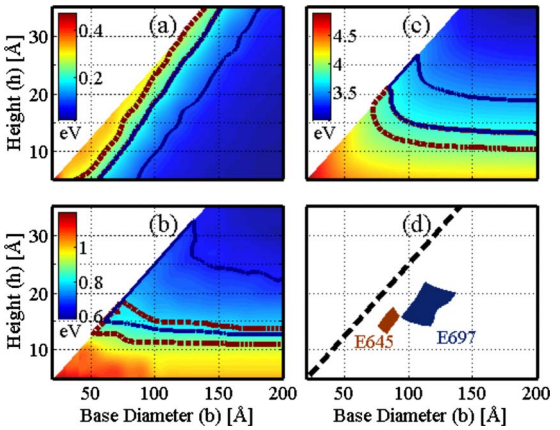

FIG. 5. (Color online) Transition energy as a function of QD height and base diameter, evaluated by effective-mass approximation for transitions: (a) S-P_x, (b) S-P_z, and (c) S-SHH. Contours mark ensembles of QD dimensions with experimentally observed transition energies: dashed lines correspond to sample E645 and full lines correspond to sample E697 measured peak energies. (d) Intersection of the ensembles marked in (a)–(c), representing the QD dimensions associated with all three experimentally observed transitions.

the GaN isotropic electron effective mass was taken as $m^*=0.2m_0$. All other material parameters can be found in Ref. 26. X-Y are the coordinates in the plane of the QD, where X is the $[11\bar{2}0]$ direction.

The effect of polarization on the band structure was taken into account by introducing a constant electric field in the Z direction. Since the QDs are in a periodic structure, we approximate the field in the QDs, F_{QD}, and in the barrier, F_B—making use of an equivalent superlattice structure[27]—as

$$F_{QD} = \frac{\Delta P}{\varepsilon_0} \frac{dB}{\varepsilon_d dB + \varepsilon_b dD},$$

$$F_B = -\frac{\Delta P}{\varepsilon_0} \frac{dD}{\varepsilon_d dB + \varepsilon_b dD}, \quad (4)$$

where ΔP is the difference between the total polarization (piezoelectric and spontaneous) of the QD and the barrier, dB is the width of the AlN spacer (3 nm) and $dD=h+\mathrm{WL}$ is the sum of the QD height h (measured from the top of the WL) and the thickness of the WL. ε_d (ε_b) is the static dielectric constant of the QD (barrier). Although the WL thickness is a free parameter of the model, it had little effect on the transition energies as long as the overall height (dD) is constant. Due to the lattice symmetry—and based on the AFM images and the spectroscopic measurements, showing no in-plane polarization sensitivity—lateral elongation was neglected. As the facets of the QDs are $\{10\bar{1}3\}$ planes, the angle θ between all facets and the pyramid base is constant and equals 32°. Thus, the QD is completely described by two parameters: the base diameter (b) and the height (h).

The calculated 3D wave functions for a QD with $h=1.5$ nm and $b=8$ nm are presented in Fig. 4. The two columns on the right show the contours of the squared absolute wave functions for the S, P_x, P_y, and P_z electron states evaluated for vertical and horizontal cross sections at locations shown in the bottom left drawings. For comparison, the first three states of the heavy holes $hh1$, $hh2$, and $hh3$, are presented in the two left columns.

Figures 5(a)–5(c) show the calculated S-P_x, S-P_z, and S-SHH transition energies, respectively, as functions of dot dimensions (h and b). SHH stands for the heavy-hole first state in the valance band (Fig. 4, top left). The diagonal left border in Fig. 5 represents the maximum h/b ratio, which is about 1/4 for $\theta=32°$. The calculated S-$P_{x,y}$ transition energy is significantly lower than that of the S-P_z transition, as observed experimentally (Fig. 3). The low symmetry in the plane of the QDs removes the degeneracy of the P_x and the P_y states. Since P_x is only a few meV lower in energy than P_y and since this splitting hardly depends on QD dimensions, the P_y state is frequently omitted.

The dashed and the full contours in Figs. 5(a)–5(c) are the outlines of the calculated dimensions of the QD ensembles for samples E645 and E697, respectively, for which transition energies were experimentally observed. The dimensions of these QD ensembles are derived based on FWHM of the peaks since broadening of the peaks is due to QD size fluctuations. The joint intersections (JIs) of the three ensembles are shown Fig. 5(d), representing the dimension range of QDs concurrently exhibiting all the measured transitions. For sample E645 (E697) the JI is the small (large) rectangle centered at a height of 1.6 nm (1.8 nm) and a base diameter of 8 nm (12 nm). In the evaluation of the S-SHH transition energy for this figure, a fitting parameter Φ was introduced, representing the effect of strain on the band gap. The value of Φ was derived to maximize the JI. Φ will be used later to compare different effective-mass models.

As seen in Fig. 5, there is a distinct difference between the S-P_z and the S-SHH equienergy lines, and that of S-P_x. While the first two [Figs. 5(b) and 5(c)] vary little with the base diameter, except for a small region near the diagonal

border, the energy of the S-P_x transition [Fig. 5(a)] is highly dependent on this diameter. As a result, S-P_x transitions around 200 meV can be observed even in QDs as large as 3 nm high and 14 nm base diameter. In comparison, the S-P_x separation energy, deduced from IB absorption measurements,[28,29] is at least five times smaller in InAs QDs, which have a smaller effective mass. In fact, the higher energy of the S-$P_{x,y}$ transition is a manifestation of the large AlN/GaN conduction-band offset and the strong polarization field that tends to "push" the electron away from the QD base. Therefore, the electron localization is enhanced by the polarization field, whereas the hole confinement—close to the QD base—is weaker. The outer contour lines in Fig. 4 (top row), enclosing 90% of the wave function, can be used as a measure of this localization. While for the hole state this contour coincides with the QD diameter (b), for the electron ground state it appears at $\sim 2b/3$.

The calculated S-P_z and S-SHH transition energies at the limit of $b \to \infty$ should be compared with experimental data for quantum wells (QWs) of width h+WL, specifically to the $e1$-$e2$ transition energy between the first and the second QW subbands and to the interband transition energy $e1$-$hh1$, respectively. Both the calculated $\lim_{b\to\infty} S$-P_z and $\lim_{b\to\infty} S$-SHH(Φ) are about 200 meV higher than the experimental $e1$-$e2$ and $e1$-$hh1$ QW data.[30] This discrepancy indicates that the effective mass is larger than that assumed by the isotropic model. However, it is impossible to reconcile all observed transition energies using a single isotropic effective mass for any given QD dimensions. By increasing the effective mass by only 10%, the maximum S-P_x transition energy over the given range of h and b is less than 220 meV, while the experimental data in the present work clearly indicate that this transition energy can be much larger. These observations show the necessity of incorporating the effective-mass anisotropy into the model since S-P_x is mostly affected by the in-plane effective mass whereas S-P_z is associated with the heavier in-growth direction effective mass. Using the inverse effective-mass tensor $(1/m^*)_{ij}$ (assumed diagonal for simplicity), Eq. (3) becomes

$$\left(-\frac{\hbar^2}{2}\sum_i \nabla \frac{1}{m^*_{ii}(x,y,z)}\nabla + V_e(x,y,z)\right)\varphi_e = E\varphi_e. \qquad (5)$$

Figure 6 shows the difference between the JI dimensions corresponding to the observed transitions evaluated by various effective-mass models. The difference between the isotropic-mass models with $m^*=0.2m_0$ [black line, same as in Fig. 5(d)] and the anisotropic one with $m^*_{xx}=m^*_{yy}=m^*_{\parallel}=0.18m_0$ and $m^*_{zz}=m^*_{\perp}=0.22m_0$ (gray line) is shown in Fig. 6(a). The effect of anisotropy on the JI can be interpreted as follows: to maintain the same transition energy with higher effective mass, the QD dimensions must be reduced. Thus, the higher effective mass in the growth direction shifts the S-P_z ensembles [contours in Fig. 5(b)] in $-\hat{h}$; however, it hardly changes the S-$P_{x,y}$ transitions energy. Therefore, the JI—determined by the intersection of the S-P_z and the S-P_x ensembles—shifts along the diagonal direction [diagonal arrow in Fig. 6(a)] dictated by the equienergy lines in Fig. 5(a). Similarly, the lower in-plane mass shifts the S-P_x ensembles

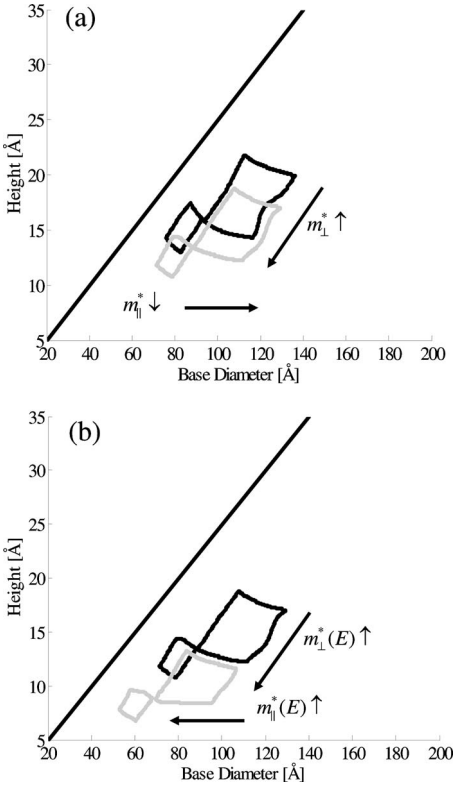

FIG. 6. Changes in JI dimensions of QDs (small squares: sample E645; large squares: sample E697) due to the incorporation of (a) anisotropic effective mass (gray line) as compared to isotropic (black line). (b) Anisotropy and nonparabolicity (gray line) as compared to anisotropy [black line, same as gray in (a)].

in the $\hat{b}$ direction. Since the S-P_z equienergy lines are horizontal, the JI also shifts in the $\hat{b}$ direction [horizontal arrow in Fig. 6(a)].

To be consistent with the QW limit, it is essential to incorporate nonparabolicity. In our model this is accomplished by taking an energy-dependent effective mass $m^*=m^*(x,y,z,E)$. Following Tchernycheva *et al.*,[30] we extracted the energy dependence of the GaN electron effective mass from the dispersion curves using an eight-band $k\cdot p$ model.[31] $m^*_{\perp}$ ($m^*_{\parallel}$) was extracted from the dispersion curve along the [0001] ([10$\bar{1}$0]) direction. The energy-dependent effective mass was then fitted to a second-degree polynomial of the form

$$m^*/m_{0k} = M^*_{0k} + M^*_{1k}(E-E_c) + M^*_{2k}(E-E_c)^2, \qquad (6)$$

where E_c stands for the GaN conduction-band edge and $k=\perp,\parallel$. Table II shows the values of the polynomial coefficients M^*_{ik}. Equations (5) and (6) have to be solved self-consistently. The numerical solution was obtained by iterations over the eigenvalues $\{E_i\}$.

Figure 6(b) shows the change in the JI dimensions evaluated by the anisotropic-mass model [black line, same as Fig. 6(a)] in comparison with the energy-dependent effective-mass model (gray line). The introduction of nonparabolicity in the z direction shifts the JI dimensions further down in the diagonal direction [diagonal arrow in Fig. 6(b)], while the

TABLE II. Second-degree polynomial coefficients of the in-plane and the out-of-plane effective masses.

	M_0^* (dimensionless)	M_1^* (eV^{-1})	M_2^* (eV^{-2})
$(m^*/m_0)_\perp$	0.22	0.068	0.003
$(m^*/m_0)_\parallel$	0.18	0.054	0.004

in-plane nonparabolicity shifts it in the $-\hat{b}$ direction [horizontal arrow in Fig. 6(b)], indicating the increase in the in-plane mass at the $P_{x,y}$ energy levels.

Table III demonstrates the influence of the different effective-mass models on the evaluated characteristic parameters. In order for the results to be consistent with the QW limit, nonparabolicity must be incorporated into the model, while introducing anisotropic effective mass is essential to obtain S-P_x transition energy in the range of 100–300 meV, in agreement with the our experimental data.

The average QD dimensions as deduced from the nonparabolic model are 6 nm (9 nm) base diameter and 0.8 nm (1.1 nm) height for sample E645 (E697). These values are significantly lower than the dimensions deduced by AFM (Table I). We attribute this difference to the inaccuracy of the AFM measurements, which results from the high QD density (in the range of 10^{12} cm^{-2}), and the convolution of the AFM tip with the small QDs, as commented in Sec. II. Indeed, HRTEM measurements, preformed on similar samples, show that the dot lateral dimensions are in the range of 5–15 nm,[18] in agreement with our model. Moreover, for the areal density in our samples, of about 10^{12} cm^{-2}, the QD diameter should be less than 10 nm.

In the evaluation of the OS by Eq. (2), the states a' and a are the full wave functions, including the Bloch and the envelope-function parts. Taking the entire electronic spectrum, the OS obeys the Thomas-Reiche-Kuhn sum rule $\Sigma_{a'}\Theta_{a'a}=1$, valid for every initial state a. The sum is taken over all final states a'. As intra-conduction-bands represent only a fraction of the electronic spectrum, the partial summation over IB transitions can exceed unity since the OS for downward transitions, associated with the emission of photons, is negative. If one uses only the envelop-function part to evaluate the OS, the momentum matrix element $\langle a'|P|a\rangle$ has to be modified. In the most general case, where the effective mass is both space and energy dependent, Sirtori *et al.*[32] showed that for intra-conduction-band transitions in QWs the momentum matrix element should be evaluated by

$$\langle a_e|p_z|a_g\rangle = \frac{1}{2}\langle\varphi_e|\frac{m_0}{m^*(z,E_e)}p_z + p_z\frac{m_0}{m^*(z,E_g)}|\varphi_g\rangle, \quad (7)$$

where $\varphi_{e(g)}$ are properly normalized envelope functions. In the case of QDs, where the inverse effective-mass tensor is diagonal, Eq. (7) becomes

$$\langle a_e|p_i|a_g\rangle = \frac{1}{2}\langle\varphi_e|\frac{m_0}{m_{ii}^*(x,y,z,E_e)}p_i + p_i\frac{m_0}{m_{ii}^*(x,y,z,E_g)}|\varphi_g\rangle, \quad (8)$$

where $p_i=p_x,p_y,p_z$. Using Eq. (8), we evaluate the OS in the X, Y, and Z directions. Figure 7 shows the scaled OS of the S-P_x transition, $\Theta^x_{S\text{-}P_x}/(m_0/M^*_{0\|})$, for light polarized in the X direction as a function of QD dimensions. Two models are compared: the one including nonparabolicity [Fig. 7(a)] and the one for anisotropic (parabolic) effective mass [Fig. 7(b)].

In order to clarify how the nonparabolicity and the internal field affect the OS, we compare the three configurations demonstrated in Figs. 7(c)–7(e) [denoted as configuration (c)–(e)]. These figures show the first three energy levels in a QD of the same height, but of different base diameters. The main difference between the three configurations is the degree of confinement of the S state with respect to the $P_{x,y}$ states, governed by a combination of the lateral dimensions and the Stark shift due to the internal field. In configuration (c), corresponding to the QDs with the smallest base diameter, there is no further confinement due to the polarization field (neither for the $P_{x,y}$ states nor for the S state); thus, the overlap between the S and the $P_{x,y}$ wave functions is the largest and the OS is the biggest. As the QD base diameter increases, the configuration evolves to (d), in which only the S state is further confined by the internal field, and thus the OS is reduced. In configuration (e) both S and $P_{x,y}$ are further confined by the field and the OS is larger than in (d). The transition from configuration (d) to (e) is marked by dotted lines in Figs. 7(a) and 7(b). Configuration (e) appears only if

TABLE III. Comparison of characteristic parameters derived with various effective-mass models.

	Φ (meV)	$\lim_{\substack{b\to\infty \\ h=0.5\ nm}} S$-$P_z$/SHH (eV)	$\lim_{\substack{b\to\infty \\ h=1\ nm}} S$-$P_z$/SHH (eV)	Average aspect ratio (h/b) E645	E697
m^*=const	370	1.1/4.32	0.95/3.94	1/5	1/6
$m^*=m^*(x,y,z)$	350	1.02/4.27	0.92/3.91	1/5	1/6
$m^*=m^*_{ii}(x,y,z)$	200	0.97/4.15	0.88/3.85	1/6	1/7
$m^*=m^*_{ii}(x,y,z,E)$	70	0.9/3.89	0.75/3.53	1/8	1/8
Experimental value	130[a]	0.92/3.92[b]	0.78/3.45[b]	1/8[c]	1/10[c]

[a]This value represents the increase in GaN band gap due to strain, evaluated by an eight-band $k\cdot p$ model (Ref. 31) for pseudomorphic biaxial strained GaN over AlN bulk.
[b]Reference 30.
[c]Deduced from AFM images.

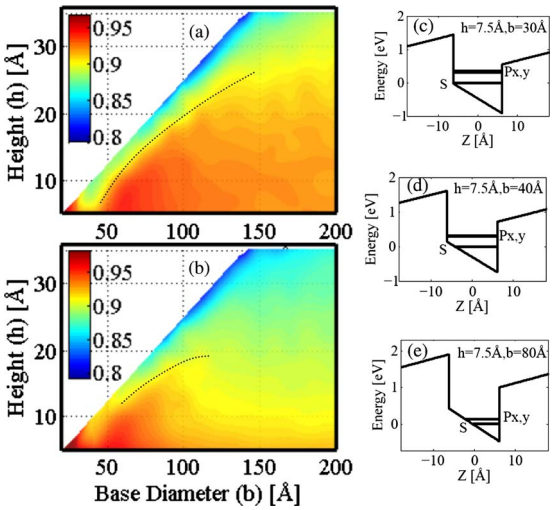

FIG. 7. (Color online) Mapping of S-P_x OS as a function of QD dimensions for two anisotropic models: upper left (a) energy-dependent effective mass (nonparabolicity); lower left (b) energy-independent effective mass. (c)–(e) show the S and the $P_{x,y}$ energy levels in QDs with the same height but different base diameters—as the base diameter becomes larger, both S and $P_{x,y}$ become strongly affected by the electric field. The dotted lines in (a) and (b) indicate the transition between configurations depicted in (d) and (e).

the QD volume is large enough. In this configuration the OS is highly sensitive to the transition energy since larger transition energy results in a reduced overlap. Increasing the QD volume by enlarging the height (with a constant base diameter) reduces its truncated top facet and increases the S-$P_{x,y}$ transition energy [see Fig. 5(a)]. Therefore, the OS decreases as h increases.

When comparing the OS obtained by the nonparabolic model with the one obtained by the parabolic model, it is important to consider the same configuration. In configuration (c), the introduction of nonparabolicity reduces the OS by about 2%, as in the field-free case. In configuration (d), since both the nonparabolicity and the internal field reduce the OS, the total reduction—due to the incorporation of nonparabolicity—is even larger. Interestingly, in configuration (e) (which covers most of the QD-size range) the OS is up to 2% larger in the nonparabolic model, in spite the increased effective mass. This is due to the fact that, for a given QD dimension, in the nonparabolic model, the S-$P_{x,y}$ transition energy is smaller (larger overlap). It should be noted that as the effective mass is position and energy dependent, the known sum rule for IB, $\Sigma_{a'}\Theta_{a'a}=m_0/m^*$, is not applicable.[32,33] Thus, the scaled OS, evaluated above for the S-P_x transition, does not represent a fraction of the total OS.

For larger QDs, the OS of the S-$P_{x,y}$ transitions is smaller. This is true also in the field-free case and in other material systems.[19] Moreover, it was shown[34] that the in-plane OS for the S-$P_{x,y}$ transitions is further increased when the spacing between QDs become smaller. Thus, when comparing the optical response of the two samples shown in Fig. 2, sample E697—in which the QDs are larger and the density is lower—is expected to show a slightly weaker response. As the optical response in the present work was characterized by transport measurements, the above observation is further supported by the fact that the tunneling probability, discussed in the next section, is also larger for small QDs.

To conclude this section we present the electronic spectra, as evaluated using the nonparabolic model, for a typical QD in sample E697 [Fig. 8(a)] and sample E645 [Fig. 8(b)], with respect to the conduction-band edge profile, in the Z direction for a cross section through the center of the QD. The figures also indicate the location of the WL (~0.5 nm wide) with a dashed line. The WL thickness is comparable to the QD vertical dimension. Thus, at the QD center, the effective width of the potential well in the growth direction is larger than the QD height, measured from the WL. Using the 3D wave functions and the energy spectrum, we evaluated the OS for all the possible transitions from the ground state S, for light polarized in X, Y, and Z directions. The resulting OS for S-$P_{x,y}$ and S-P_z transitions is presented in Fig. 8 on a logarithmic scale (inset). The asymmetry in the Z direction, due to the polarization field, gives rise to a somewhat richer spectrum for Z polarized light. Thus, the OS for the S-P_z transition is reduced with respect to S-P_x, P_y.

The main transition for Z polarized light is S-P_z for the JI dimensions (defined above) in both samples. All the other possible transitions in the Z direction are significantly weaker. Calculation of the average value of the OS over the JI of both samples for the S-P_z transition renders 0.75 m_0/m^*, which is the value used earlier to estimate the number of electrons per dot. Figures 8(c) and 8(d) show the 2D absorption coefficient, given by Eq. (1), for all the calculated levels of the simulated structures. In this calculation we assumed a QD density of 10^{12} cm^{-2} and a Lorentzian line shape with a FWHM of 20 meV representing the lifetime broadening.

A comparison between the absorption in Fig. 8(d) and the photoresponse in Fig. 3(a) emphasizes the unique nature of the experimental results: while the S-P_z absorption is roughly the same as S-$P_{x,y}$, the photocurrent due to the S-P_z absorption is an order of magnitude larger. This aspect of the result is discussed in detail in the next section.

B. Electronic transport

In most QDIPs, room-temperature conductivity is due to thermionic or field emission processes.[35] In AlN/GaN QDIPs, the strong localization, induced by the large band offset, impedes free-carrier transport. This localization is evident by the intense photoluminescence observed up to 750 K.[36] Nevertheless, lateral transport in AlN/GaN QDIPs may be facilitated by high QD density. In our case, the average distance between nearest-neighbor QDs is about 10 nm and the QD lateral dimension is 6–9 nm; therefore, the AlN barriers in the plane of the QDs are 1–4 nm and interdot tunneling is likely. The high density of QDs is essential for transport in our devices, as evidenced by the absence of conductivity in the reference sample (discussed in Sec. II) which contains no QDs.

An insight to the origin of the observed photocurrent, due to BtB transitions within the QDs, is obtained by investigating the transport mechanism in highly localized systems. As

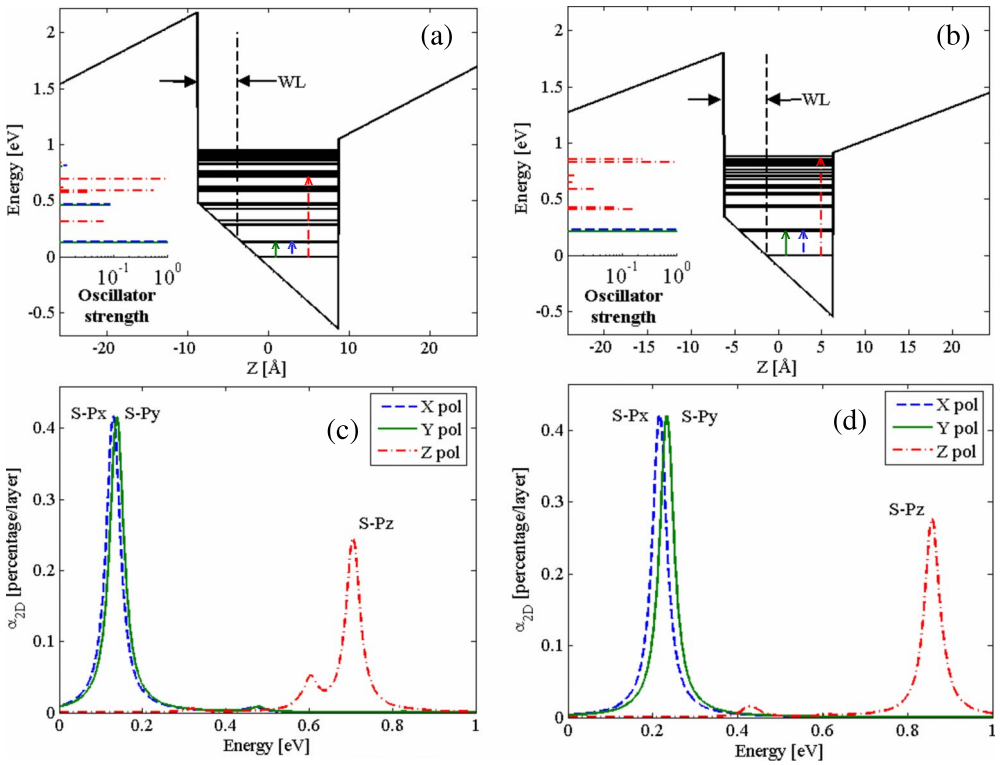

FIG. 8. (Color online) Electronic energy level schemes of two QDs, displayed in a cross section of conduction band in the Z (growth) direction through QD center, evaluated using an energy-dependent effective-mass model. Energy levels of: (a) 1.25-nm-high and 9-nm-base-diameter QD, corresponding to sample E697, and (b) QD of 0.75 nm high and 6 nm base diameter, corresponding to sample E645. Inset: scaled OS from S state for X (dashed blue line), Y (full green line), and Z (dotted-dashed red) polarizations ($\log_{10}$ scale). (c) and (d) Absorption of a single layer of QDs corresponding to spectra presented in (a) and (b), respectively, calculated for QD density of 10^{12} cm^{-2} and Lorentzian line shape with FWHM of 20 meV.

the optical excitation, in our case, does not generate free carriers and the number of trapped carriers in the system does not change, the photocurrent must be related to the change in transport properties (mobility) as carriers are excited into different states within the QDs.

Transport between localized states originates from a sequence of tunneling events between two sites, known as hopping conductivity. The hopping process is governed by the transition rate from site i, with energy E_i, to a distant site j with energy E_j. This rate is often described by the Miller-Abrahams model[37]

$$\omega_{ij} = \gamma \begin{cases} e^{-2R_{ij}/\xi} e^{-(E_j - E_i)/kT}, & E_j \geq E_i \\ e^{-2R_{ij}/\xi}, & E_j < E_i, \end{cases} \tag{9}$$

where γ is a parameter related to the attempt frequency and weakly depends on temperature, k is the Boltzmann constant, and T is the temperature. In Eq. (9), $e^{-2R_{ij}/\xi}$ represents the tunneling probability, with R_{ij} being the physical distance separating the two sites and ξ being the localization length of the sites. In general, ξ is determined by the potential surrounding the hopping sites and is directly related to the barrier height. Thus, a larger ξ associated with shallower levels represents an increase in the hopping probability. The hopping rate depends exponentially on ξ; therefore, small changes in ξ can lead to measurable changes in conductance.

At low temperature, the states are filled up to the Fermi level. Thus, hopping is possible only to sites with equal or higher energies ($E_j \geq E_i$), and the hopping rate decreases exponentially with the host site energy E_j [Eq. (9)]. In contrast, under illumination, carriers are excited into levels which are clearly above the Fermi energy, hence, enabling hopping into lower energy levels ($E_j < E_i$). Therefore, the maximum rate is achieved by hopping into nearest neighbors. Assuming that ξ is the main factor controlling the transport of optically excited carriers, and that the nearest-neighbor distance is $\sim$10 nm, the ratio between the NIR peak intensity (associated with transport of carriers in the P_z state) to the MIR peak intensity (associated with transport of carriers in the $P_{x,y}$ states, see Fig. 3) leads to a difference of 0.11 nm^{-1} between the P_z and the $P_{x,y}$ localization parameters ($\alpha \equiv 1/\xi$). This value sets an upper limit of 9 nm on the localization length for QDs contributing to the photoresponse. This result is in a good quantitative agreement with the lateral dimensions of the QDs as derived from the simulations.

The behavior of the localization parameter as a function of energy depends on the dimensions of the system. In one dimension (1D), the localization parameter follows $\sqrt{2m^*(V-E)}/\hbar$, where V is the critical energy, taken with respect to the bottom of the quantum structure. V is referred to as the mobility edge, above which the states are extended.

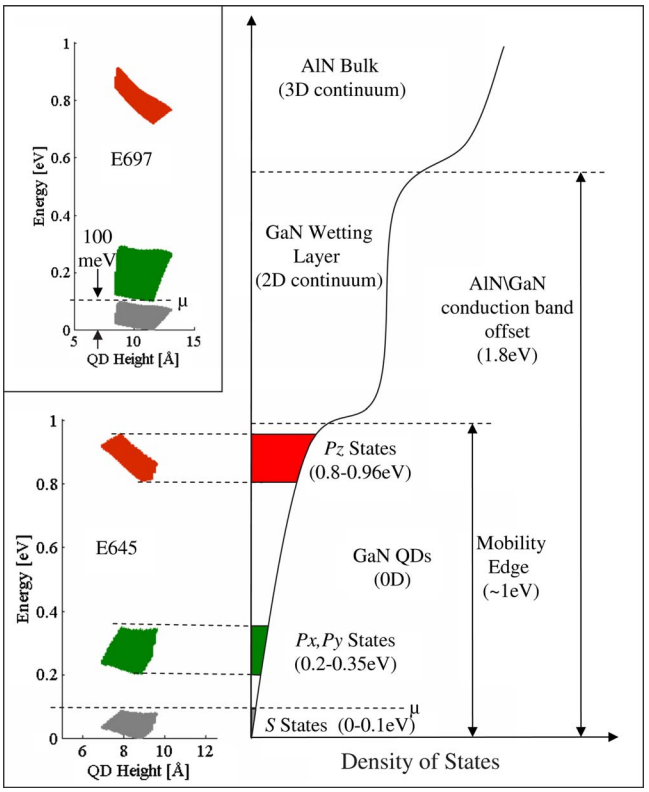

FIG. 9. (Color online) Schematic of density of states, showing evaluated mobility edge and AlN/GaN conduction-band offset. Left section: broadening of S, P_x, and P_z states energies due to QD size inhomogeneity, evaluated for sample E645 using energy-dependent effective-mass model. Inset: same as the left section, evaluated for sample E697.

For higher dimensions, based on dimensionality considerations, Mott found[38]

$$1/\xi = 1/\xi_0 \left(\frac{V-E}{V} \right)^s, \tag{10}$$

where ξ_0 is the localization length far below the mobility edge and $s=1$ ($s=2/3$) in two (three) dimensions. Taking ξ_0 as the length in which 90% of the S wave function is localized in the X-Y plane, we numerically evaluated $\xi_0=5$ nm for a 6-nm-base-diameter and 1.1-nm-high QD (the average QD dimensions in sample E645 as deduced from the nonparabolic model). Using Eq. (10) to evaluate the mobility edge based on the difference between the localization parameters of the P_z and the $P_{x,y}$ states, we find that $V \cong 1$ eV. This value, being smaller than the conduction-band offset between GaN and AlN (1.8 eV), indicates that extended states above V exist within the two-dimensional WL. The 2D mobility edge can also be estimated by evaluating the energy of the first subband in a quantum well of a width equal to the WL thickness ($\sim$0.5 nm) with respect to the average QD ground states. This approach leads to a mobility edge at $\sim$0.8 eV.[9] Figure 9 shows schematically the density of states in the conduction band. In addition, the figure shows the energy range of S, $P_{x,y}$, and P_z states of the QD JI (defined in Sec. IV A) in sample E645, which reflects inhomogeneous broadening due to size fluctuations. It is apparent both from the simulations and from the evaluation of the mobility edge that the P_z states are 3D confined, unlike P_z states in similar InGaAs/GaAs QDs, which usually extend in two dimensions.[23] The 3D confinement of the P_z states is a direct consequence of the large GaN/AlN band offset and the conduction-band nonparabolicity which strongly affects the S-P_z transition energy. As P_z exhausts most of the out-of-plane OS, no transitions to the WL quasicontinuum could be resolved.

The inset of Fig. 9 shows the S, $P_{x,y}$, and P_z states corresponding to QD JI of sample E697. As all QDs in the intersection show absorption, the Fermi level must at least coincide with the highest S state of the intersection, marked by μ in the figure and in the inset. While in sample E645 μ is significantly lower than the $P_{x,y}$ range, in sample E697 the $P_{x,y}$ range is partially overlapping the S range. This finding may account for the fact that, while in sample E645 the MIR photoresponse gradually disappears with decreasing energy, in sample E697 there is an abrupt cutoff at about 100 meV (Fig. 2), as QDs in this sample with S-$P_{x,y}$ separation smaller than 100 meV are filled up to $P_{x,y}$ inclusively.

In order to further characterize the transport mechanism, we measured the temperature dependence of the dark current. In dark conditions, hopping is possible mostly into higher energy [$E_j \geq E_i$ in Eq. (9)] and the conductivity is determined by the average transport properties of carriers within kT around the Fermi level. As in our case the Fermi level is much lower than the continuum, VRH behavior can be expected. In VRH, there is a competition between the two exponential factors in Eq. (9). The first factor $e^{-2R_{ij}/\xi}$, related to the tunneling probability, increases as R_{ij} decreases. The second factor $e^{-(E_j-E_i)/kT}$, related to the activation energy, increases with R_{ij} [$W_{ij} \equiv E_i - E_j \sim 1/f(R_{ij})$, where $f(R_{ij})$ is a monotonically increasing function of R_{ij}]. Thus, there is an optimal hopping distance which maximizes the hopping rate. In his pioneer work on VRH,[15] based on statistical argument, Mott derived an expression for $f(R_{ij})$. In Mott's VRH (M-VRH) model, the typical energy required for hopping of carrier from a site with energy i to a distant site j within a sphere of radius R_{ij} is given by $W_{ij}=1/\beta R_{ij}^d N_F$,[15] where d stands for the dimensionality; N_F is the density of states at the Fermi level, assumed to be constant; and β is a numeric constant. Based on the above relation, one finds that the optimal hopping distance is $\bar{R}=(\xi/\beta N_F kT)^{1/(d+1)}$. Therefore, there is a critical temperature, $T^*=\xi/\beta k N_F R_{NN}^{d+1}$, for which the optimal hopping distance $\bar{R}$ is equal to the nearest-neighbor distance $R_{NN}=1/\sqrt{N_{QD}}$, where N_{QD} is the QD areal density. For temperatures higher than T^*, the transport is via nearest-neighbor hopping (NNH). In this regime the first factor in Eq. (9) is constant ($e^{-2R_{NN}/\xi}$); thus, the conductivity follows a simple activation process with a typical activation energy $W_{NNH} \sim 1/f(R_{NN})$. Below T^*, carriers may optimize their paths using VRH, resulting in a weaker temperature dependence. Using $\bar{R}$ in Eq. (9), Mott found a temperature-dependent conductance of the form $\exp(-(T_0/T)^{1/(d+1)})$, where $T_0=3^{d+1}/\beta N_F \xi^d$. The dimensionality of the system is governed by the ratio between the thickness of the media and the hopping distance. Since, in our case, the GaN epilayer

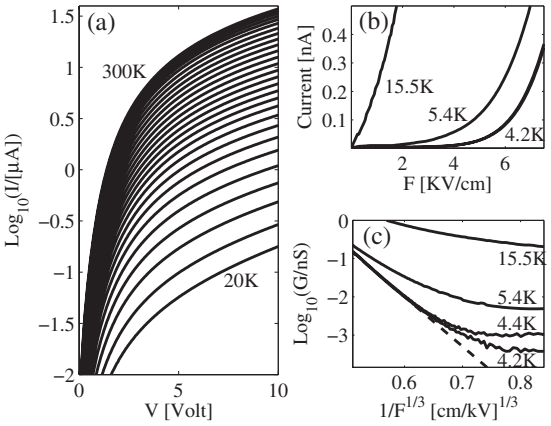

FIG. 10. Dark current characteristics for sample E645 at various temperatures: (a) from 300 to 20 K (logarithmic scale), (b) from 15.5 to 4.2 K, and (c) field-dependent conductance from 4.2 to 15.5 K.

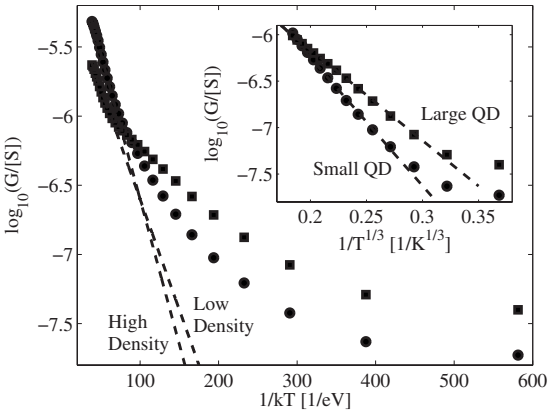

FIG. 11. Dark conductance vs $1/kT$ for samples E645 (small QDs) and E697 (large QDs). Inset: conductance vs $1/T^{1/3}$ for both samples.

thickness is about five times smaller than the nearest-neighbor distance, the system is considered 2D.

Figure 10(a) shows the current-voltage characteristics measured on sample E645 in dark conditions as a function of temperature, from 300 to 20 K, at every 10 K. The dark current decreases monotonically as the temperature is lowered. In our experimental setup, only when the dark current is smaller than a few tens of nA (below 20 K) the MIR photocurrent could be spectrally resolved.

Figure 11 compares the dark conductance of the two samples as a function of temperature at low bias ($FR_{NN}=1$ meV$\ll kT$, where F stands for electric field). At higher temperatures the conductance follows an activation behavior as expected in the NNH regime. Below 150 K (170 K) in sample E645 (E697), the temperature dependence becomes weaker as carriers optimize their path via VRH. The inset of Fig. 11 shows $\log_{10}(G)$ as a function of $1/T^{1/3}$, indicating that the conductance at temperatures higher than ~50 K follows the 2D M-VRH behavior. Table IV summarizes the characteristic temperature T_0 at the M-VRH regime, the activation energy W_{NNH} at the NNH regime, and the crossover temperature T^* obtained on samples E645 and E697. W_{NNH} and T_0 were extracted from the data using least-squares fitting.

The differences between the characteristics parameters, shown in table IV, are due to the difference in dimensions and densities of the QDs between the two samples. The ratio $T_0^{E697}/T_0^{E645}=(\xi^{E645}/\xi^{E697})^2$ results in the ratio $\xi^{E645}=0.6\xi^{E697}$ between the localization lengths of the two samples. This indicates that the QDs in sample E645 are smaller than those in sample E697, in accordance with all other experimental evidence. T^* (the crossover to NNH) is governed by $\xi/R_{NN}^3=\xi N_{QD}^{3/2}$; thus, the ratio $T^{*E697}/T^{*E645}=(\xi^{E697}/\xi^{E645})(N_{QD}^{E697}/N_{QD}^{E645})^{3/2}$ renders $N_{QD}^{E697}=0.77N_{QD}^{E645}$, in qualitative agreement with the QD density as measured by AFM. At the NNH regime, the activation energy is inversely proportional to the nearest-neighbor distance R_{NN},[39] which is consistent with the larger activation energy (W_{NNH}) in sample E645 (where R_{NN} is smaller).

TABLE IV. Fitted parameters for dark conductance in samples E645 and E697.

	W_{NNH} (meV)	T^* (K)	T_0 (K)
E645	21	150	2571
E697	16	170	941

The conductance follows M-VRH behavior in the range of 150 to ~50 K. Below 50 K, FR_{NN} becomes comparable to kT and the conductance behavior depends both on the temperature and the electric field, resulting in a deviation from the $1/T^{-1/3}$ dependence (inset of Fig. 11). Further lowering the temperature [Fig. 10(b)], $FR_{NN}\gg kT$ and the field becomes the dominant source of energy for hopping. Thus, one can relate W_{ij} to the electric field via $W_{ij}=qR_{ij}F=1/\beta R_{ij}^d N_F$, which results in a field-dependent hopping distance (in the field direction) of $R_F=(q\beta F N_F)^{-1/d+1}$. Using R_F to express the hopping rate, one finds a field-dependent conductance of the form $\exp(-(F_0/F)^{1/(d+1)})$, where the characteristic field is given by $F_0=2^{d+1}/\beta q N_F \xi^{d+1}$. Note that, at this regime, the conductivity is no longer temperature dependent. To validate this behavior, we characterized the dark current at liquid-helium temperature. Figures 10(b) and 10(c) show the dark current and the conductance as functions of electric field, respectively, measured on sample E645. As the temperature is lowered the low field conductance practically vanishes. However, as the field becomes strong enough, the current increases exponentially. The least-squares fitting of $\log_{10}(G)$ vs $F^{-1/3}$ at 4.2 K yields a characteristic field of $F_0=2197$ kV/cm. It can be seen that, for all temperatures in the range of 4–15 K, the conductance asymptotically approaches the $F^{-1/3}$ dependence at high enough fields.

V. CONCLUSIONS

We studied IB transitions in the IR spectral range in GaN/AlN QDs using in-plane electronic transport at low temperatures. Based on structural measurements, polarization analy-

sis of the spectral response, and theoretical model considerations, we were able to characterize BtB transitions within the QDs conduction band. The photocurrent due to such transitions—showing sensitivity to the size of QDs and to the states into which carriers are excited—is a direct consequence of the high density of QDs in the studied samples, which allows hopping transport to take place. The photocurrent mechanism is further supported by the dark current temperature dependence showing several characteristics of hopping and also sensitive to the QD size and density.

The optical response at MIR wavelengths is associated with BtB transitions from the ground state S to the first two exited states P_x and P_y. The measurable change in the conductance resulting from these internal transitions in the QDs was explained by means of modulation of the hopping probability by the optical excitation. Based on the ratio between the NIR photocurrent intensity, attributed to transport of carriers following an S-P_z excitation, and the MIR photocurrent intensity, associated with carrier transport following an S-$P_{x,y}$ excitation, a 2D mobility edge at $\sim$1 eV above the GaN conduction-band edge was derived. This means that for the given QD dimensions the P_z level is 3D confined, and further improvement in the transport of P_z excited carriers can be achieved by using smaller QDs (for shorter wavelengths) or by reducing the band offset between the QD and barriers.

The S-$P_{x,y}$ energy separation in GaN/AlN QDs, characterized in this work, is significantly larger than the equivalent transition energy in In(Ga)As/GaAs QDs. The analysis shows that the appearance of large energy S-$P_{x,y}$ in GaN/AlN QDs is due to the strong internal electric field in the QDs which results in a stronger confinement of the electrons at the QD top facet. The electron localization in the QDs is also manifested by the sample transport properties, with a dark current inversely proportional to the QD density at room temperature.

ACKNOWLEDGMENTS

We would like to acknowledge the financial support of EC FP7 FET project "UNITRIDE" Contract No. 233950. This work was supported, in part, also by the United States-Israel Binational Science Foundation (BSF) under grant Contract No. 2004366. The AlN-on-sapphire templates used as substrates were supplied by DOWA Electronic Materials. The authors acknowledge the assistance of Abdo Baleegh in cryogenic measurements.

*Corresponding author; valon@tx.technion.ac.il

[1] D. Bimberg, M. Grundmann, and N. N. Ledentsov, *Quantum Dot-Heterostructures* (Wiley, Chichester, 1999).
[2] Y. Arakawa and H. Sakaki, Appl. Phys. Lett. **40**, 939 (1982).
[3] Z. Yuan, B. E. Kardynal, R. M. Stevenson, A. J. Shields, C. J. Lobo, K. Cooper, N. S. Beattie, D. A. Ritchie, and M. Pepper, Science **295**, 102 (2002).
[4] S. Kako, C. Santori, K. Hoshino, S. Gotzinger, Y. Yamamoto, and Y. Arakawa, Nature Mater. **5**, 887 (2006).
[5] M. Tchernycheva, L. Nevou, L. Doyennette, A. Helman, R. Colombelli, F. H. Julien, F. Guillot, E. Monroy, T. Shibata, and M. Tanaka, Appl. Phys. Lett. **87**, 101912 (2005).
[6] S. C. Bunce, M. Izzetoglu, K. Izzetoglu, B. Onaral, and K. Pourrezaei, IEEE Eng. Med. Biol. Mag. **25**, 54 (2006).
[7] N. Iizuka, K. Kaneko, and N. Suzuki, IEEE J. Quantum Electron. **42**, 765 (2006).
[8] N. Kheirodin, L. Nevou, H. Machhadani, P. Crozat, L. Vivien, M. Tchernycheva, A. Lupu, F. H. Julien, G. Pozzovivo, S. Golka, G. Strasser, F. Guillot, and E. Monroy, IEEE Photonics Technol. Lett. **20**, 724 (2008).
[9] A. Vardi, N. Akopian, G. Bahir, L. Doyennette, M. Tchernycheva, L. Nevou, F. H. Julien, F. Guillot, and E. Monroy, Appl. Phys. Lett. **88**, 143101 (2006).
[10] A. Vardi, G. Bahir, F. Guillot, C. Bougerol, E. Monroy, S. E. Schacham, M. Tchernycheva, and F. H. Julien, Appl. Phys. Lett. **92**, 011112 (2008).
[11] H. C. Liu and H. Schneider, *Quantum Well Infrared Photodetectors Physics and Applications* (Springer, Berlin, 2007).
[12] L. Fu, H. H. Tan, I. McKerracher, J. Wong-Leung, C. Jagadish, N. Vukmirovic, and P. Harrison, J. Appl. Phys. **99**, 114517 (2006).
[13] H. Z. Song, K. Akahane, S. Lan, H. Z. Xu, Y. Okada, and M. Kawabe, Phys. Rev. B **64**, 085303 (2001).
[14] A. I. Yakimov, C. J. Adkins, R. Boucher, A. V. Dvurechenskii, A. I. Nikiforov, O. P. Pchelyakov, and G. Biskupski, Phys. Rev. B **59**, 12598 (1999).
[15] N. F. Mott, J. Non-Cryst. Solids **1**, 1 (1968).
[16] V. Chamard, T. Schulli, M. Sztucki, T. H. Metzger, E. Sarigiannidou, J. L. Rouviere, M. Tolan, C. Adelmann, and B. Daudin, Phys. Rev. B **69**, 125327 (2004).
[17] E. Sarigiannidou, E. Monroy, B. Daudin, J. L. Rouviere, and A. D. Andreev, Appl. Phys. Lett. **87**, 203112 (2005).
[18] F. Guillot, E. Bellet-Amalric, E. Monroy, M. Tchernycheva, L. Nevou, L. Doyennette, F. H. Julien, D. Le Si, T. Remmele, M. Albrecht, T. Shibata, and M. Tanaka, J. Appl. Phys. **100**, 044326 (2006).
[19] A. Vasanelli, M. De Giorgi, R. Ferreira, R. Cingolani, and G. Bastard, Physica E **11**, 41 (2001).
[20] A. Vasanelli, R. Ferreira, and G. Bastard, Phys. Rev. Lett. **89**, 216804 (2002).
[21] G. Yu, G. Wang, H. Ishikawa, M. Umeno, T. Soga, T. Egawa, J. Watanabe, and T. Jimbo, Appl. Phys. Lett. **70**, 3209 (1997).
[22] L. Chu, A. Zrenner, G. Bohm, and G. Abstreiter, Appl. Phys. Lett. **76**, 1944 (2000).
[23] S. W. Lee, K. Hirakawa, and Y. Shimada, Appl. Phys. Lett. **75**, 1428 (1999).
[24] S. Maimon, E. Finkman, G. Bahir, S. E. Schacham, J. M. Garcia, and P. M. Petroff, Appl. Phys. Lett. **73**, 2003 (1998).
[25] D. El-Moghraby, R. G. Johnson, and P. Harrison, Comput. Phys. Commun. **150**, 235 (2003).
[26] I. Vurgaftman and J. R. Meyer, J. Appl. Phys. **94**, 3675 (2003).
[27] F. Bernardini and V. Fiorentini, Appl. Surf. Sci. **166**, 23 (2000).

[28] E. A. Zibik, L. R. Wilson, R. P. Green, G. Bastard, R. Ferreira, P. J. Phillips, D. A. Carder, J-P. R. Wells, J. W. Cockburn, M. S. Skolnick, M. J. Steer, and M. Hopkinson, Phys. Rev. B **70**, 161305(R) (2004).

[29] S. Sauvage, P. Boucaud, R. P. S. M. Lobo, F. Bras, G. Fishman, R. Prazeres, F. Glotin, J. M. Ortega, and J.-M. Gérard, Phys. Rev. Lett. **88**, 177402 (2002).

[30] M. Tchernycheva, L. Nevou, L. Doyennette, F. H. Julien, E. Warde, F. Guillot, E. Monroy, E. Bellet-Amalric, T. Remmele, and M. Albrecht, Phys. Rev. B **73**, 125347 (2006).

[31] E. Berkowicz, D. Gershoni, G. Bahir, E. Lakin, D. Shilo, E. Zolotoyabko, A. C. Abare, S. P. Denbaars, and L. A. Coldren, Phys. Rev. B **61**, 10994 (2000).

[32] C. Sirtori, F. Capasso, J. Faist, and S. Scandolo, Phys. Rev. B **50**, 8663 (1994).

[33] D. P. Dave and H. F. Taylor, Phys. Lett. A **184**, 301 (1994).

[34] V. G. Stoleru and E. Towe, Appl. Phys. Lett. **83**, 5026 (2003).

[35] H. Lim, W. Zhang, S. Tsao, T. Sills, J. Szafraniec, K. Mi, B. Movaghar, and M. Razeghi, Phys. Rev. B **72**, 085332 (2005).

[36] J. Brown, C. Elsass, C. Poblenz, P. M. Petroff, and I. S. Speck, Phys. Status Solidi B **228**, 199 (2001).

[37] M. Pollak and B. I. Shklovskii, *Hopping Transport in Solids* (Elsevier, North-Holland, Amsterdam, 1991).

[38] N. F. Mott, Commun. Phys. **1**, 203 (1976).

[39] F. Shimogishi, K. Mukai, S. Fukushima, and N. Otsuka, Phys. Rev. B **65**, 165311 (2002).